Enhanced Performance and Stability of 3D/2D Tin Perovskite Solar Cells Fabricated with a Sequential Solution Deposition

Efat Jokar, Po-Yuan Cheng, Chia-Yi Lin, Sudhakar Narra, Saeed Shahbazi, and Eric Wei-Guang Diau*

Read Online

ACCESS | Metrics & More | Article Recommendations | SI Supporting Information

ABSTRACT: To solve the toxic issue for new-generation photovoltaic applications, tin-based perovskite solar cells are a promising alternative to their lead counterparts, but they suffer from poor stability because of their tendency to exhibit tin oxidation. Herein we report a new sequential method of deposition based on solution processing using hexafluoro-2-propanol as a solvent to deposit eight bulky ammonium cations on top of the 3D layer to form a 3D/quasi-2D layer to protect the tin perovskite grains from penetration by moisture. The formation of the 2D layer was confirmed with grazing-incidence wide-angle X-ray scattering, scanning electron microscopy, conducive atomic force microscopy, photoluminescence, and transient absorption spectroscopy measurements. The anilinium (AN) device showed a remarkable performance with an efficiency of 10.6% and with great stability in ambient air without encapsulation. The AN device also showed a self-healing effect of performance when it was subjected to a severe environment under continuous light soaking in one-sun illumination and thermal stress between 20 and 50 °C for 10 cycles.
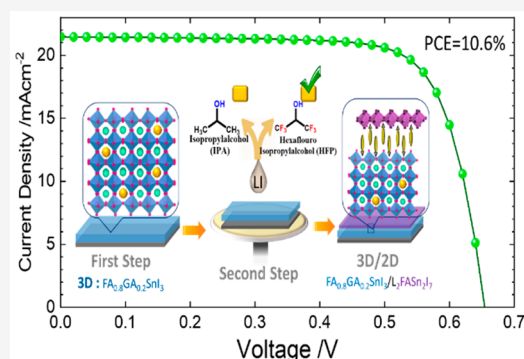
Tin-based perovskite solar cells (PSCs) have attracted considerable attention because of their rapid progress as an alternative to solve the toxic problem of their lead-based analogues.[1−4] Their stability, however, becomes an issue for such tin-based PSCs because tin(II) tends to oxidize to form defects of tin vacancies in the crystal, resulting in nonradiative charge recombination that deteriorates their device performance.[5−7] To suppress the Sn^{2+}/Sn^{4+} oxidation, strategies such as additives or co-additives,[8−10] co-cations,[4,11,12] mixed anions,[13,14] and low-dimensional (LD) hybrid structures[15−17] have been developed for tin-based PSCs. Among those strategies, the LD perovskite layers with two-dimensional (2D) or quasi-2D structures play an important role in protecting the tin perovskite layer from moisture and thus suppress the oxidation of tin(II) so as to enhance the device performance and stability. Most 3D/2D tin-based PSC devices were fabricated on adding bulky ammonium cations (BACs), e.g., butylammonium (BA),[8] phenylethylammonium (PEA),[17,18] and so on, into the formamidinium tin triiodide ($FASnI_3$) precursor solution according to a one-step procedure so that the growth orientation and the location of the 2D/quasi-2D layer were difficult to control. For lead-based PSCs, a bilayer 3D/2D structure was introduced with a sequential deposition to grow the 2D layer on top of the 3D layer using a typical solvent, isopropanol (IPA).[19−21] This two-step method

might not, however, work well because IPA may destroy the tin perovskite film in the second step, as mentioned elsewhere.[22−26] Although there has been one report of tin-based PSCs using a PEABr/IPA treatment in the second step to obtain 7.86% efficiency of power conversion (PCE),[27] the stability of the tin perovskite film remains an issue to be resolved. In a recent report, 4-(trifluoromethyl)benzyl ammonium/chloroform was used in the second step to obtain a PCE of 10.96%.[28] However, chloroform is a nonpolar solvent for its limitation to dissolve most organic ammonium cations easily.[29]

One solution to prepare the 3D/2D tin perovskite bilayer via a sequential fabrication approach is to use the vapor deposition method where no solvent was involved in the second step of deposition.[30] However, vapor deposition is an expensive method in terms of the costs of the equipment and the starting materials. In the present work, we introduce a promising sequential solution-processed approach to generate
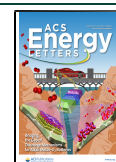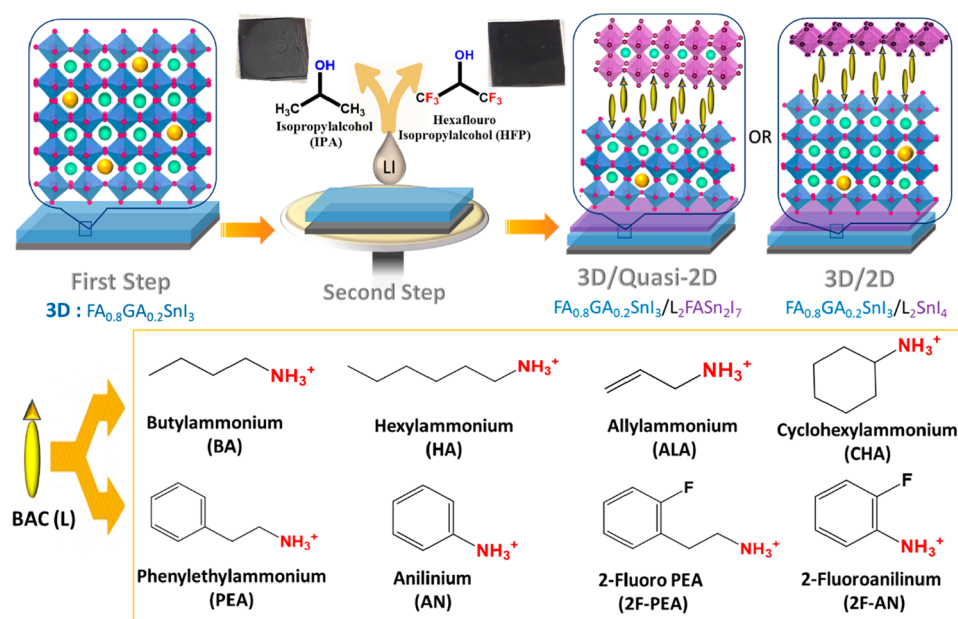
Figure 1. Schematic representation of sequential deposition to grow a low-dimensional perovskite phase on the 3D layer ($FA_{0.8}GA_{0.2}SnI_3$, abbreviated as E1G20) in the second step using one of eight bulky ammonium cations (BAC, represented by L) as indicated. The top photographs show the effect of solvents (left, IPA; right, HFP) applied in the second step to dissolve the LI salts.
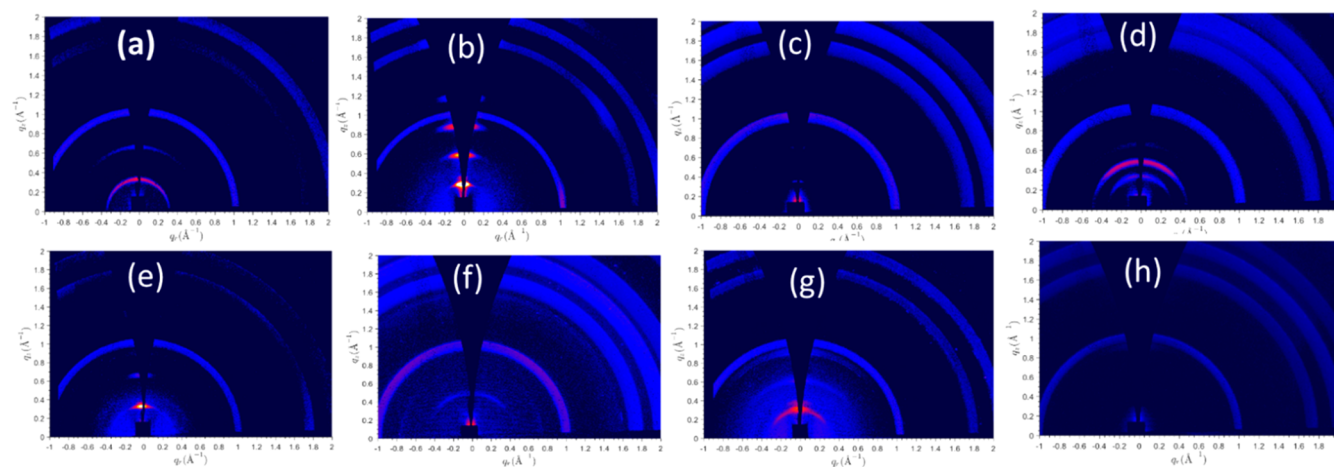

Figure 2. 2D GIWAXS patterns of 3D/2D tin perovskite films fabricated with (a) BA, (b) HA, (c) ALA, (d) CHA, (e) PEA, (f) AN, (g) 2F-PEA, and (h) 2F-AN at incident angle α = 0.2°.

the 3D/2D tin-perovskite bilayer with great device performance and superior stability in ambient air without encapsulation, as well as under thermal stress and light-soaking conditions. As shown in Figure 1, the 3D tin perovskite, $GA_{0.2}FA_{0.8}SnI_3$-1% $EDAI_2$ (E1G20; GA represents guanidinium; $EDAI_2$ represents ethylenediammonium iodide), was produced in a one-step method reported elsewhere.[11] To grow the 2D/quasi-2D layer, we used hexafluoro-2-propanol (HFP) instead of IPA as a solvent in the second step to deposit eight BACs, such as BA, hexylammonium (HA), allylammonium (ALA), cyclohexylammonium (CHA), PEA, anilinium (AN), 2-fluoro-PEA (2F-PEA), and 2F-AN, on top of the E1G20 layer. This step introduces a general sequential method under solution processing to produce a stable 3D/2D bilayer for tin-based PSC application, for which the AN device attained remarkable PCE of 10.6% with significantly enhanced open-circuit voltage (V_{OC} = 0.66 V). Here, the chemistry of the bulky organic cation was studied systematically.

The challenge to make a stable 3D/2D bilayered tin perovskite using sequential deposition is to find a suitable solvent in the second step that can dissolve the BAC but does not destroy the 3D perovskite film.[26] As mentioned previously, using solvent IPA in the second step[27] might damage the 3D tin perovskite film, even during spin-coating, as the photograph shows in Figure 1. In fact, the tin perovskite film was completely destroyed when pure IPA was dropped on top of its surface after 20 s. In contrast, the tin perovskite film remained in a black phase when the dropped HFP was completely evaporated in a glovebox, as shown in Figure S1. The images from scanning electron microscopy (SEM) shown in Figure S2 indicate that the IPA-treated E1G20 film displays pinholes, whereas the HFP-treated film shows a uniform morphology free of pinholes. HFP is hence an appropriate solvent to produce a uniform 3D/2D tin-perovskite film according to the sequential procedure shown in Figure 1.
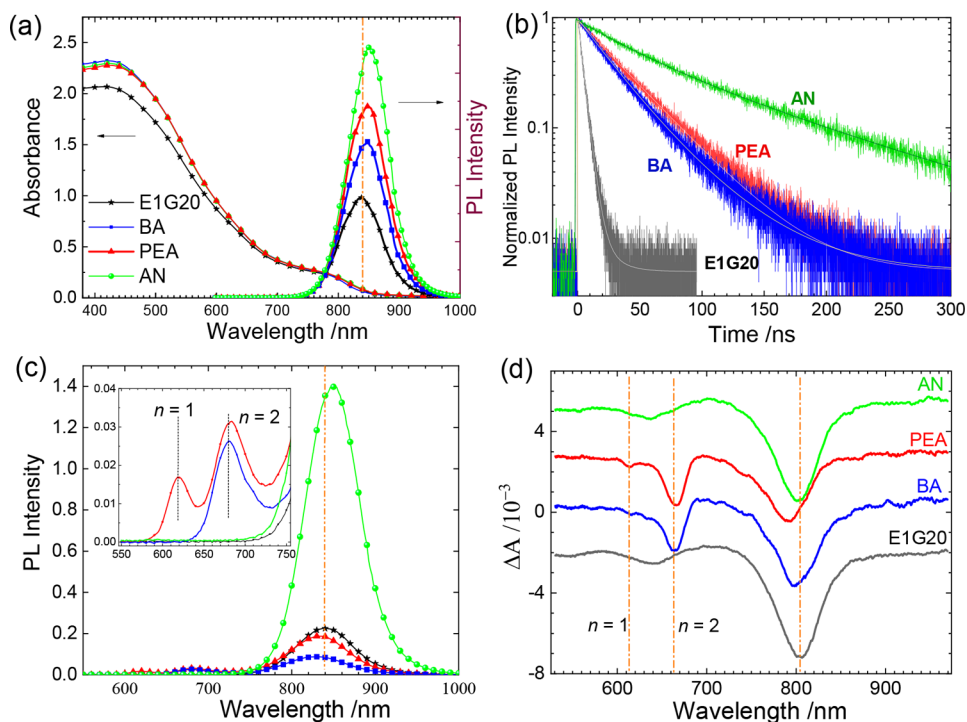
Figure 3. Optical characterization of (a) steady-state absorption and photoluminescent (PL) spectra and (b) PL decay profiles with excitation at λ_{ex} = 450 nm and concentration 7.5 mM, and those of (c) PL spectra ps (λ_{ex} = 450 nm) and (d) fs transient absorption spectroscopy (TAS) at delay 5 ps (λ_{ex} = 520 nm) at concentration 30 mM of the LI solution for E1G20, BA, PEA, and AN films as indicated.

HFP has six fluorine atoms attracting electrons to act as an acid that interacts with BAC to slow the reaction on the surface of a 3D tin perovskite to form a 2D layer (L_2SnI_4) and/or a quasi-2D layer ($L_2FA_{n-1}Sn_nI_{3n+1}$, $n > 1$) on top of the E1G20 layer; L represents one of eight BAC linkers (Figure 1), classified as aliphatic (BA, HA, ALA, and CHA) and aromatic (PEA, AN, 2F-PEA, and 2F-AN) groups. To investigate the LD perovskite phases and crystal orientation, we measured grazing-incidence wide-angle X-ray scattering (GIWAXS) results for each cation. The 2D GIWAXS patterns at incident angle α = 0.2° shown in Figure 2 represent scattering on the surface of the films made of eight BACs; the corresponding GIWAXS patterns at incident angle α = 2° shown in Figure S3 represent the scattering in the bulk. For the 3D E1G20 film, only Debye–Scherrer rings appear in the GIWAXS (Figure S4). In contrast, additional incomplete rings or spots along an out-of-plane direction (q_z) at $q_z < 1$ was observed for the films made of BAC. The GIWAXS data were obtained at concentration of 30 mM of LI because the 2D/quasi-2D patterns at 7.5 mM of LI were nearly imperceptible, as the data of the PEA films show in Figure S5. The plots of integrated scattering intensities along the q_z-direction shown in Figure S6 confirm this feature and provide strong evidence for the formation of a 2D/quasi-2D layer on top of the 3D layer as a result of our sequential deposition.

Bulky cations BA, PEA, and AN were considered for further characterization because they represent ammonium functional groups with aliphatic (BA), aromatic (PEA), and conjugated aromatic (AN) side chains attached. Top-view SEM images in Figure S7 visualize the morphologies of the 3D/2D layers. The morphology of the AN film is similar to that of the E1G20 film; the morphologies of BA and PEA films are only slightly altered, with tiny nanostructures covering the crystal grains at a small concentration, reflecting the growth of a thin 2D layer on top

of the 3D layer. In contrast, the polycrystalline feature of the 3D layer was completely covered with an aggregated 2D layer for the BA and PEA films under the condition of the larger concentration. For the AN film, the morphology at the larger concentration is similar to that at the smaller concentration; that film is smoother than all other films (Figure S8). Our SEM results are also complementary to explain the GIWAXS data for the formation of an ultrathin 2D layer scarcely perceptible for the AN and 2F-AN films, even at a large concentration. Further analysis was carried out using conducive atomic force microscopy (c-AFM) under high vacuum to avoid any oxidation or morphology change on the sample surface. c-AFM images of the E1G20 and AN samples in low concentration (7.5 mM) are shown in Figure S8. Topographic images (Figure S8a,d) show the AN sample is smoother than the E1G20 sample, which agrees well with the SEM images. The corresponding current distributions in E1G20 between grains show an inhomogeneous feature (Figure S8b,c), and the photocurrents dropped significantly at the grain boundaries. In contrast, for the AN sample, the photocurrent distributions are more uniform with little variations between grain boundary and grain interior regions (Figure S8e,f). These results indicate that the thin 2D layer was formed to cover the boundaries of the 3D grains for the enhanced photoconductivities observed for the AN sample.

We undertook optical measurements to verify the kind of LD phase formed in those BAC films at low and high concentrations. Figure 3a shows steady-state UV–visible absorption and photoluminescence (PL) spectra under backside excitation (the 2D side) for the E1G20, BA, PEA, and AN sample at concentration of 7.5 mM; those of other 3D/2D films are shown in Figure S9 for comparison. The absorption spectra of the BAC films are all similar to each other, whereas the PL spectra display a slight bathochromic
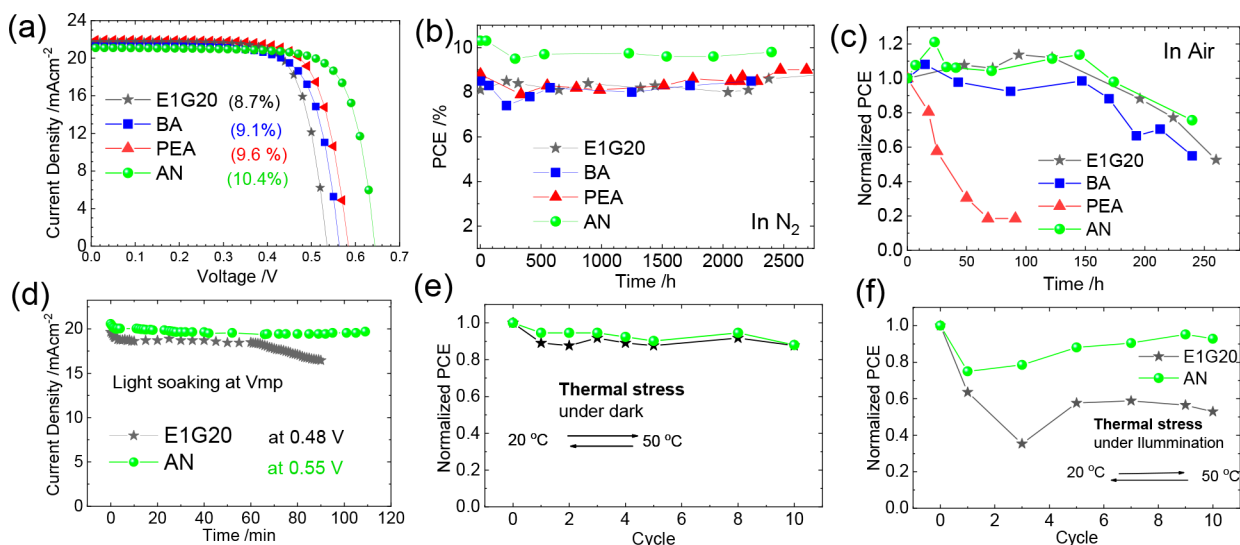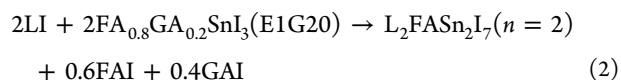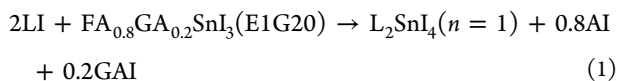
Figure 4. (a) Current−voltage characteristics, (b) PCE vs storage period for encapsulated devices kept in a N_2-filled glovebox in darkness, (c) normalized PCE vs storage period for unencapsulated devices in ambient air conditions (RH = 40%), (d) current density vs time for a light-soaking test of an encapsulated device at the maximum power point (V_{mp}) in ambient air conditions, and normalized PCE vs heating−cooling cycle for thermal-stress tests of encapsulated devices in ambient air conditions (e) in darkness and (f) under one-sun illumination.

shift (∼10 nm) with the PL intensities showing the trend AN > PEA > BA > E1G20. The PL decay profiles obtained from the TCSPC measurements appear in Figure 2b; the corresponding decay coefficients are listed in Table S1. The E1G20 sample has an average lifetime of ∼5 ns; introducing an additional 2D layer enhanced significantly the lifetimes to 34 ns (BA), 42 ns (PEA), and 105 ns (AN), consistent with the trend observed for the PL intensities shown in Figure 3a. We attribute this enhancement of the PL intensities and lifetimes of the 3D/2D samples to suppression of the defect states of the E1G20 film in the presence of the 2D layer. In addition, passivation of the grain surface of the E1G20 film might occur via these BACs to produce lower trap states, which are dark upon excitation while they are emissive after relaxation, responsible for the red shifts of the PL spectra observed in Figure 3a.

To confirm the phases of the 2D layer, we performed steady-state PL and transient absorption spectral (TAS)[7] measurements for the three samples at concentration of 30 mM, for which aggregated 2D structures were formed in larger amounts on BA and PEA samples. The PL (Figures 3c and S10) and TAS (Figures 3d and S11) spectra of the PEA sample show the formation of the 2D ($n = 1$) and quasi-2D ($n = 2$) phases, whereas those of the BA sample show only a formation of the quasi-2D ($n = 2$) phase. The same phenomenon was observed for the PL spectra of HA (vs BA) and 2F-PEA (vs PEA) shown in Figure S10. Panels a and b of Figure S12 show the PL and TAS spectra, respectively, to compare the spectral feature of the BA sample with those of the pure BA_2SnI_4 ($n = 1$) and $BA_2FASn_2I_7$ ($n = 2$) films. The $n = 2$ peaks of the PL and TAS spectra of the BA sample show a blue-shifted feature with respect to those of the pure $BA_2FASn_2I_7$ sample due to the involvement of the GA cation that increases the bandgap energy as reported elsewhere.[11] We hence propose the following chemical equations for the formation of phases $n = 1$ and $n = 2$ via the reaction of LI with E1G20:

$$2LI + FA_{0.8}GA_{0.2}SnI_3(E1G20) \rightarrow L_2SnI_4(n = 1) + 0.8AI$$
$$+ 0.2GAI \qquad (1)$$

$$2LI + 2FA_{0.8}GA_{0.2}SnI_3(E1G20) \rightarrow L_2FASn_2I_7(n = 2)$$
$$+ 0.6FAI + 0.4GAI \qquad (2)$$

in which L represents BAC, except for films AN and 2F-AN of which the 2D structural features were nearly imperceptible in the PL, TAS, SEM, and GIWAXS results. Phase $n = 2$ is the most favorable quasi-2D structure according to our sequential deposition because it is an equimolar reaction (eq 2) between LI and E1G20, as shown in the BA and HA samples. A large concentration of BAC might induce, however, the formation of phase $n = 1$, as shown in the PEA and 2F-PEA samples. There is a slight hypsochromic shift for the 3D signals in PL and TAS spectra for both BA and PEA samples at the larger concentration, indicating the formation of quasi-2D phases at orders $n > 2$. In contrast, Figure 3a shows a slight bathochromic shift for the PL spectra of the 3D/2D samples taken at lower BAC concentration, because of the aforementioned effect of surface passivation.

The 3D/2D PSC were fabricated according to our sequential deposition based on device architecture ITO/PEDOT:PSS/perovskite (3D/2D)/C60/BCP/Ag reported previously.[11] We have characterized device performance for all eight BACs and optimized the performance of the AN device at varied concentrations; the best device was found at concentration 7.5 mM (Figure S13). The current−voltage ($J−V$) characteristics of E1G20, BA, PEA, and AN are shown in Figure 4a; the corresponding IPCE spectra are shown in Figure S14. The $J−V$ characteristics of HA, CHA, ALA, 2F-PEA, and 2F-AN are shown in Figure S15. The best performance of a fresh E1G20 device that served as a standard cell was obtained with PCE of 8.7%; those of the BA (9.1%), PEA (9.6%), AN (10.4%), ALA (9.3%), and 2F-AN (8.9%) are superior to that of the standard cell, but those of HA (8.4%), CHA (7.8%), and 2F-PEA (8.3%) are slightly poorer (Table S2). We notice that the V_{oc} of the AN device was enhanced significantly compared to other devices. Electrochemical impedance spectroscopy (EIS) measurements were carried out to examine the effect of V_{oc} enhancement of the AN device; the corresponding results are shown in Figure S16. The EIS results indicate that the

charge recombination resistances of the AN device are much greater than those of the E1G20 device, confirming that the enhanced V_{oc} of the former is due to the passivation effect of thin 2D layer on perovskite surface. The box plots (Figure S17; the corresponding raw data are in Tables S3−S11) show satisfactory reproducibility of these devices. The device performance in relation to their molecular structures and optical properties are discussed as three points in what follows.

We first compare the device performance for the aliphatic group, with the performance trend of ALA > BA > HA > CHA. The 2D structures of BA have been widely investigated;[30−32] only phase n = 2 (together with uncertain minor high-order phases) was produced on the bulk E1G20 layer. The GIWAXS data (Figure 2) show that the quasi-2D layers of BA and CHA were randomly oriented; as CHA has a much stronger surface-scattering signal than BA, the CHA film is too thick to obtain a satisfactory performance. In contrast, the 2D GIWAXS patterns were scarcely perceptible for the ALA film; this thin-layer feature endowed the ALA device with a performance slightly better than the BA device. With a longer alkyl chain in HA, a stronger GIWAXS signal was observed, showing the growth direction of the 2D crystal to be parallel to the substrate plane on top of the 3D layer. Both CHA (randomly orientated) and HA (horizontally oriented) films are thus so thick that they form a blocking layer to degrade the device performance.

Second, we compare the device performance for the aromatic group, for which the trend of performance is AN > PEA > 2F-AN > 2F-PEA. An additional fluorine atom was added in 2F-PEA and 2F-AN to increase the hydrophobicity of the 2D layer for the purpose of enhanced stability. The fluorine substitution results in worse performance than their non-substituted counterparts; crystallographic disorder might be introduced by the fluorine atom.[33] PEA has been broadly applied in a one-step approach to grow the 2D and quasi-2D layer perpendicular to the substrate plane because π-electrons can decrease the barrier between the inorganic and organic frames and enhance the charge transport.[34−37] This π−π interaction thus plays an important role to form a well-oriented 2D layer.[38−40] In our case, the post-treatment of PEA in the second step produced phases both n = 1 and n = 2 (with minor high-order phases) parallel to the substrate plane that can improve the device performance from PCE of 8.7% (E1G20) to 9.6%. In the AN case, a thin 2D layer of phase n = 1 was produced to passivate grain boundaries of the E1G20 film and reduce iodide and tin vacancies on the surface, which give remarkable overall performance, PCE of 10.4%. The XPS spectra of the AN and E1G20 films are shown in Figure S18, for which both tin and iodine atomic ratios significantly increased for the AN film in comparison that for the E1G20 film.

Third, CHA has size and rigidity similar to AN, but its device performance is much poorer.[41] In addition to the π−π interaction of the aromatic groups, the acidity must be considered for the superior performance of the AN device.[40,42] Because the ammonium group is directly attached to the phenyl ring, the π-conjugation of the electrons in the N atom of the AN cation with those in the phenyl ring leads to delocalization of the charges and thus decreased the charge density at the N atom to make the cation AN a strong acid (pK_a = 4.6 vs 9.8 for PEA).[43] In contrast, the deprotonated HFP with six fluorine atoms make it a strong base. AN and deprotonated HFP might thus form a stable Lewis acid−base

complex to retard the crystal growth of LD phases so as to form a thinner layer and not to impede the charge transport among the crystal grains. To prove the interaction of AN with HFP, NMR experiments for AN dissolved in IPA and HFP were undertaken; the results and interpretation appear in Figure S19.

We tested the performance stability of the devices under five conditions: dark storage (i) in a N_2 environment and (ii) in ambient air for E1G20, BA, PEA, and AN; (iii) light soaking at maximum power point (V_{mp}) for E1G20 and AN; thermal stress (iv) in darkness and (v) under one-sun illumination for E1G20 and AN; the corresponding results are shown in Figure 4b−f. The encapsulated devices were stable over 2000 h when they were stored in darkness in a glovebox (Figure 4b); the effect of slow passivation is perceptible for the E1G20 device as reported previously.[8] To leave the devices in air (RH = 40%, T = 20 °C) without encapsulation is, however, a challenging task. E1G20, BA, and AN devices retained their original performance unencapsulated in air for over 150 h and then began to degrade, whereas the PEA device deteriorated rapidly in the first 70 h (Figure 4c). This observed degradation of performance might be due to the 2D layer of PEA containing phases both n = 1 and n = 2 and destroying the 3D/2D interface so that water and oxygen penetrate into the hybrid structure. In contrast, a formation of a pure and thin 2D layer in BA (n = 2) and AN (n = 1) protects the device from moisture penetration and shows excellent stability, like lead-based PSC. For the AN device, we found a slight improvement of the device performance during the first few days when an unencapsulated device was stored in air (Figure S20). V_{OC} increased upon storage period from 0 h (∼0.6 V) to 200 h (∼0.7 V); both short-circuit current density (J_{SC}) and fill factor (FF) first increased but then decreased after 50 h. As a result, the best performance of the AN device was obtained at the storage period ∼80 h, for which PCE 10.6% was obtained. These results indicate that slow passivation also occurred in air without encapsulation, and water and oxygen can assist surface passivation for an AN device for a few days.

The AN and E1G20 devices were chosen for further tests of stability under conditions of light soaking and thermal stress. Each device was encapsulated and measured under ambient air conditions. Figure 4d shows the stabilized current density under one-sun illumination at the V_{mp} point. Under these conditions, the E1G20 device was stable for 1 h before the current began to decrease. In contrast, the AN device retained its original performance for more than 100 min. We notice that the temperature increased substantially during light soaking for 1 h, and this led to oxidation of the silver electrode for further extending the stability period at the V_{mp} condition. The great stability of AN enabled us to perform strict tests on the effect of thermal stress. To our knowledge, the thermal stress has not been tested for tin-based PSCs. Here, 10 cycles of heating (50−55 °C) and cooling (20 °C) were imposed on the encapsulated AN and E1G20 devices under ambient air either in darkness (Figure 4e) or under one-sun illumination (Figure 4f). Even though the E1G20 device showed stability comparable with that of the AN device under a thermal stress in darkness, the performance degradation was more significant for the former than for the latter under one-sun illumination. Under conditions of both thermal stress and light soaking, the device performance of AN at first degraded to 80% of its initial PCE and then recovered to almost 95% after 10 cycles. This phenomenon reflects not only the superior stability of the AN

device but also a *self-healing* ability. The effect of self-healing is unclear; we speculate that it might come from surface passivation of the crystal grains in a combined light-soaking and thermal stress condition. In other words, the defects of tin perovskite crystals were initially created by light irradiation (one sun) under high temperature (50 °C) and then the cool– hot cycles made the ANI salt decompose and generate HI to passivate the grain surface of E1G20 crystal. The formation of a thin 2D layer on the 3D grain boundaries thus plays a key role in improving the stability and enhancing the performance of the 3D/2D devices fabricated using our sequential deposition.

In conclusion, we developed a sequential method of solution processing to fabricate hybrid 3D/2D tin-based perovskite solar cells with great device performance and stability. The FA/GA co-cationic 3D film (E1G20) was prepared according to a one-step procedure reported elsewhere.[11] The 2D layer was deposited on top of the 3D layer via spin-coating of varied BACs dissolved in HFP rather than the traditional solvent IPA, which could destroy the tin perovskite film as reported elsewhere.[26] Using HFP as a solvent in the second step of deposition would induce a strong interaction between BAC and HFP to slow the reaction of BAC with the E1G20 film and to produce a thin layer of a 2D ($n = 1$) phase or a quasi-2D phase, confirmed with investigations of GIWAXS, *c*-AFM, SEM, PL, and TAS. Among all eight BACs under investigation, anilinium (AN) was found to form an ultrathin 2D ($n = 1$) layer on the surface and between the grain boundaries to protect the tin perovskite layer from moisture penetration so as to enhance the device performance to attain PCE of 10.6%. The unencapsulated AN device is stable under ambient air (RH 40%, $T = 20$ °C) over 150 h; a *self-healing* effect on performance was found for the encapsulated AN cell under continuous one-sun illumination and thermal stress between 20 and 50 °C for 10 cycles. The present work thus provides a new route for the development of lead-free perovskite solar cells using a sequential procedure for future commercialization.

■ ASSOCIATED CONTENT

Ⓢ Supporting Information

The Supporting Information is available free of charge at https://pubs.acs.org/doi/10.1021/acsenergylett.0c02305.

> Experimental details; supplementary photos, plots, spectra, and tables (PDF)

■ AUTHOR INFORMATION

Corresponding Author

Eric Wei-Guang Diau − *Department of Applied Chemistry and Institute of Molecular Science, National Chiao Tung University, Hsinchu 30010, Taiwan; Center for Emergent Functional Matter Science, National Chiao Tung University, Hsinchu 30010, Taiwan;* ⓞ orcid.org/0000-0001-6113-5679; Email: diau@mail.nctu.edu.tw

Authors

Efat Jokar − *Department of Applied Chemistry and Institute of Molecular Science, National Chiao Tung University, Hsinchu 30010, Taiwan; Center for Emergent Functional Matter Science, National Chiao Tung University, Hsinchu 30010, Taiwan*

Po-Yuan Cheng − *Department of Applied Chemistry and Institute of Molecular Science, National Chiao Tung University, Hsinchu 30010, Taiwan*

Chia-Yi Lin − *Department of Applied Chemistry and Institute of Molecular Science, National Chiao Tung University, Hsinchu 30010, Taiwan*

Sudhakar Narra − *Department of Applied Chemistry and Institute of Molecular Science, National Chiao Tung University, Hsinchu 30010, Taiwan;* ⓞ orcid.org/0000-0003-4893-9204

Saeed Shahbazi − *Department of Applied Chemistry and Institute of Molecular Science, National Chiao Tung University, Hsinchu 30010, Taiwan*

Complete contact information is available at:
https://pubs.acs.org/10.1021/acsenergylett.0c02305

Notes
The authors declare no competing financial interest.

■ ACKNOWLEDGMENTS

■ REFERENCES

(1) Hasan, S. A. U.; Lee, D. S.; Im, S. H.; Hong, K.-H. Present Status and Research Prospects of Tin-based Perovskite Solar Cells. *Sol. RRL* **2020**, *4*, 1900310.

(2) Diau, E. W.-G.; Jokar, E.; Rameez, M. Strategies To Improve Performance and Stability for Tin-Based Perovskite Solar Cells. *ACS Energy Lett.* **2019**, *4*, 1930−1937.

(3) Nasti, G.; Abate, A. Tin Halide Perovskite ($ASnX_3$) Solar Cells: A Comprehensive Guide toward the Highest Power Conversion Efficiency. *Adv. Energy Mater.* **2020**, *10*, 1902467.

(4) Nishimura, K.; Kamarudin, M. A.; Hirotani, D.; Hamada, K.; Shen, Q.; Iikubo, S.; Minemoto, T.; Yoshino, K.; Hayase, S. Lead-Free Tin-Halide Perovskite Solar Cells with 13% Efficiency. *Nano Energy* **2020**, *74*, 104858−104868.

(5) Meggiolaro, D.; Ricciarelli, D.; Alasmari, A. A.; Alasmary, F. A. S.; De Angelis, F. Tin versus Lead Redox Chemistry Modulates Charge Trapping and Self-Doping in Tin/Lead Iodide Perovskites. *J. Phys. Chem. Lett.* **2020**, *11*, 3546−3556.

(6) Nakamura, T.; Yakumaru, S.; Truong, M. A.; Kim, K.; Liu, J.; Hu, S.; Otsuka, K.; Hashimoto, R.; Murdey, R.; Sasamori, T.; Kim, H. D.; Ohkita, H.; Ohkita, H.; Handa, T.; Wakamiya, A. Sn(IV)-Free Tin Perovskite Films Realized by in Situ Sn(0) Nanoparticle Treatment of the Precursor Solution. *Nat. Commun.* **2020**, *11*, 3008.

(7) Narra, S.; Jokar, E.; Pearce, O. M.; Lin, C.-Y.; Fathi, A.; Diau, E. W.-G. Femtosecond Transient Absorption Spectra and Dynamics of Carrier Relaxation of Tin Perovskites in the Absence and Presence of Additives. *J. Phys. Chem. Lett.* **2020**, *11*, 5699−5704.

(8) Jokar, E.; Chien, C. H.; Fathi, A.; Rameez, M.; Chang, Y. H.; Diau, E. W.-G. Slow Surface Passivation and Crystal Relaxation with Additives to Improve Device Performance and Durability for Tin-Based Perovskite Solar Cells. *Energy Environ. Sci.* **2018**, *11*, 2353−2362.

(9) Wang, T.; Tai, Q.; Guo, X.; Cao, J.; Liu, C.-K.; Wang, N.; Shen, D.; Zhu, Y.; Lee, C.-S.; Yan, F. Highly Air-Stable Tin-Based Perovskite Solar Cells through Grain-Surface Protection by Gallic Acid. *ACS Energy Lett.* **2020**, *5*, 1741–1749.

(10) Liu, X.; Wang, Y.; Wu, T.; He, X.; Meng, X.; Barbaud, J.; Chen, H.; Segawa, H.; Yang, X.; Han, L. Efficient and Stable Tin Perovskite Solar Cells Enabled by Amorphous-Polycrystalline Structure. *Nat. Commun.* **2020**, *11*, 2678.

(11) Jokar, E.; Chien, C. H.; Tsai, C. M.; Fathi, A.; Diau, E. W.-G. Robust Tin-Based Perovskite Solar Cells with Hybrid Organic Cations to Attain Efficiency Approaching 10%. *Adv. Mater.* **2019**, *31*, 1804835.

(12) Liu, X.; Yan, K.; Tan, D.; Liang, X.; Zhang, H.; Huang, W. Solvent Engineering Improves Efficiency of Lead-Free Tin-Based Hybrid Perovskite Solar Cells beyond 9%. *ACS Energy Lett.* **2018**, *3*, 2701–2707.

(13) Rameez, M.; Shahbazi, S.; Raghunath, P.; Lin, M. C.; Hung, C. H.; Diau, E. W.-G. Development of Novel Mixed Halide/Superhalide Tin-Based Perovskites for Mesoscopic Carbon-Based Solar Cells. *J. Phys. Chem. Lett.* **2020**, *11*, 2443–2448.

(14) Rameez, M.; Lin, E. Y.-R.; Raghunath, P.; Narra, S.; Song, D.; Lin, M.-C.; Hung, C.-H.; Diau, E. W.-G. Development of Hybrid Pseudohalide Tin Perovskites for Highly Stable Carbon-Electrode Solar Cells. *ACS Appl. Mater. Interfaces* **2020**, *12*, 21739–21747.

(15) Jiang, X.; Wang, F.; Wei, Q.; Li, H.; Shang, Y.; Zhou, W.; Wang, C.; Cheng, P.; Chen, Q.; Chen, L.; Ning, Z. Ultra-High Open-Circuit Voltage of Tin Perovskite Solar Cells via an Electron Transporting Layer Design. *Nat. Commun.* **2020**, *11*, 1245.

(16) Cao, D. H.; Stoumpos, C. C.; Yokoyama, T.; Logsdon, J. L.; Song, T.-B.; Farha, O. K.; Wasielewski, M. R.; Hupp, J. T.; Kanatzidis, M. G. Thin Films and Solar Cells Based on Semiconducting Two-Dimensional Ruddlesden-Popper $(CH_3(CH_2)_3NH_3)_2(CH_3NH_3)_{n-1}Sn_nI_{3n+1}$ Perovskites. *ACS Energy Lett.* **2017**, *2*, 982–990.

(17) Wang, F.; Jiang, X.; Chen, H.; Shang, Y.; Liu, H.; Wei, J.; Zhou, W.; He, H.; Liu, W.; Ning, Z. 2D-Quasi-2D-3D Hierarchy Structure for Tin Perovskite Solar Cells with Enhanced Efficiency and Stability. *Joule* **2018**, *2*, 2732–2743.

(18) Shao, S.; Liu, J.; Portale, G.; Fang, H.-H.; Blake, G. R.; ten Brink, G. H.; Koster, L. J. A.; Loi, M. A. Highly Reproducible Sn-Based Hybrid Perovskite Solar Cells with 9% Efficiency. *Adv. Energy Mater.* **2018**, *8*, 1702019.

(19) Liu, Y.; Akin, S.; Pan, L.; Uchida, R.; Arora, N.; Milić, J. V.; Hinderhofer, A.; Schreiber, F.; Uhl, A. R.; Zakeeruddin, S. M.; Hagfelt, A.; Dar, M. I.; Gratzel, M. Ultrahydrophobic 3D/2D Fluoroarene Bilayer-Based Water-Resistant Perovskite Solar Cells with Efficiencies Exceeding 22%. *Sci. Adv.* **2019**, *5*, No. eaaw2543.

(20) Liu, Y.; Akin, S.; Hinderhofer, A.; Eickemeyer, F. T.; Zhu, H.; Seo, J.; Zhang, J.; Schreiber, F.; Zhang, H.; Zakeeruddin, S. M.; Hagfelt, A.; Dar, M. I.; Gratzel, M. Stabilization of Highly Efficient and Stable Phase-Pure FAPbI$_3$ Perovskite Solar Cells by Molecularly Tailored 2D-Overlayers. *Angew. Chem., Int. Ed.* **2020**, *59*, 15688–15694.

(21) Cho, K. T.; Grancini, G.; Lee, Y.; Oveisi, E.; Ryu, J.; Almora, O.; Tschumi, M.; Schouwink, P. A.; Seo, G.; Heo, S.; Park, J.; Jang, J.; Paek, S.; Garcia-Belmonte, G.; Nazeeruddin, M. K. Selective Growth of Layered Perovskites for Stable and Efficient Photovoltaics. *Energy Environ. Sci.* **2018**, *11*, 952–959.

(22) Konstantakou, M.; Stergiopoulos, T. A Critical Review on Tin Halide Perovskite Solar Cells. *J. Mater. Chem. A* **2017**, *5*, 11518–11549.

(23) Gu, F.; Zhao, Z.; Wang, C.; Rao, H.; Zhao, B.; Liu, Z.; Bian, Z.; Huang, C. Lead-Free Tin-Based Perovskite Solar Cells: Strategies Toward High Performance. *Sol. RRL* **2019**, *3*, 1900213.

(24) Ke, W.; Stoumpos, C. C.; Kanatzidis, M. G. Unleaded" Perovskites: Status Quo and Future Prospects of Tin-Based Perovskite Solar Cells. *Adv. Mater.* **2019**, *31*, 1803230.

(25) Hao, F.; Stoumpos, C. C.; Guo, P.; Zhou, N.; Marks, T. J.; Chang, R. P. H.; Kanatzidis, M. G. Solvent-Mediated Crystallization of CH$_3$NH$_3$SnI$_3$ Films for Heterojunction Depleted Perovskite Solar Cells. *J. Am. Chem. Soc.* **2015**, *137*, 11445–11452.

(26) Shahbazi, S.; Li, M.-Y.; Fathi, A.; Diau, E. W.-G. Realizing a Cosolvent System for Stable Tin-Based Perovskite Solar Cells Using a Two-Step Deposition Approach. *ACS Energy Lett.* **2020**, *5*, 2508–2511.

(27) Liao, M.; Yu, B.; Jin, Z.; Chen, W.; Zhu, Y.; Zhang, X.; Yao, W.; Duan, T.; Djerdj, I.; He, Z. Efficient and Stable FASnI$_3$ Perovskite Solar Cells with Effective Interface Modulation by Low-Dimensional Perovskite Layer. *ChemSusChem* **2019**, *12*, 5007–5014.

(28) Wu, T.; Cui, D.; Liu, X.; Meng, X.; Wang, Y.; Noda, T.; Segawa, H.; Yang, X.; Zhang, Y.; Han, L. Efficient and Stable Tin Perovskite Solar Cells Enabled by Graded Heterostructure of Light-Absorbing Layer. *Sol. RRL* **2020**, *4*, 2000240.

(29) Yoo, J. J.; Wieghold, S.; Sponseller, M. C.; Chua, M. R.; Bertram, S. N.; Hartono, N. T. Pu.; Tresback, J. S.; Hansen, E. C.; Correa-Baena, J.-P.; Bulvoic, V.; Buonassisi, T.; Shin, S. S.; Bawendi, M. G. An interface stabilized perovskite solar cell with high stabilized efficiency and low voltage loss. *Energy Environ. Sci.* **2019**, *12*, 2192–2199.

(30) Choi, W. G.; Park, C. G.; Kim, Y.; Moon, T. Sn Perovskite Solar Cells via 2D/3D Bilayer Formation through a Sequential Vapor Process. *ACS Energy Lett.* **2020**, *5*, 3461–3467.

(31) Bala, A.; Kumar, V. Role of Ligand-Ligand Interactions in the Stabilization of Thin Layers of Tin Bromide Perovskite: An Ab Initio Study of the Atomic and Electronic Structure, and Optical Properties. *J. Phys. Chem. C* **2019**, *123*, 25176–25184.

(32) Stoumpos, C. C.; Cao, D. H.; Clark, D. J.; Young, J.; Rondinelli, J. M.; Jang, J. I.; Hupp, J. T.; Kanatzidis, M. G. Ruddlesden-Popper Hybrid Lead Iodide Perovskite 2D Homologous Semiconductors. *Chem. Mater.* **2016**, *28*, 2852–2867.

(33) Hu, J.; Oswald, I. W. H.; Stuard, S. J.; Nahid, M. M.; Zhou, N.; Williams, O. F.; Guo, Z.; Yan, L.; Hu, H.; Chen, Z.; et al. Synthetic Control over Orientational Degeneracy of Spacer Cations Enhances Solar Cell Efficiency in Two-Dimensional Perovskites. *Nat. Commun.* **2019**, *10*, 1276.

(34) Passarelli, J. V.; Fairfield, D. J.; Sather, N. A.; Hendricks, M. P.; Sai, H.; Stern, C. L.; Stupp, S. I. Enhanced Out-of-Plane Conductivity and Photovoltaic Performance in n = 1 Layered Perovskites through Organic Cation Design. *J. Am. Chem. Soc.* **2018**, *140*, 7313–7323.

(35) Li, X.; Ke, W.; Traoré, B.; Guo, P.; Hadar, I.; Kepenekian, M.; Even, J.; Katan, C.; Stoumpos, C. C.; Schaller, R. D.; et al. Two-Dimensional Dion-Jacobson Hybrid Lead Iodide Perovskites with Aromatic Diammonium Cations. *J. Am. Chem. Soc.* **2019**, *141*, 12880–12890.

(36) Mauck, C. M.; Tisdale, W. A. Excitons in 2D Organic–Inorganic Halide Perovskites. *Trends in Chemistry* **2019**, *1*, 380–393.

(37) El-Ballouli, O.; Bakr, O. M.; Mohammed, O. F. Structurally Tunable Two-Dimensional Layered Perovskites: From Confinement and Enhanced Charge Transport to Prolonged Hot Carrier Cooling Dynamics. *J. Phys. Chem. Lett.* **2020**, *11*, 5705–5718.

(38) Quintero-Bermudez, R.; Gold-Parker, A.; Proppe, A. H.; Munir, R.; Yang, Z.; Kelley, S. O.; Amassian, A.; Toney, M. F.; Sargent, E. H. Compositional and Orientational Control in Metal Halide Perovskites of Reduced Dimensionality. *Nat. Mater.* **2018**, *17*, 900–907.

(39) Chen, A. Z.; Shiu, M.; Deng, X.; Mahmoud, M.; Zhang, D.; Foley, B. J.; Lee, S.-H. H.; Giri, G.; Choi, J. J. Understanding the Formation of Vertical Orientation in Two-Dimensional Metal Halide Perovskite Thin Films. *Chem. Mater.* **2019**, *31*, 1336–1343.

(40) Rodríguez-Romero, J.; Hames, B. C.; Mora-Seró, I.; Barea, E. M. Conjugated Organic Cations to Improve the Optoelectronic Properties of 2D/3D Perovskites. *ACS Energy Lett.* **2017**, *2*, 1969–1970.

(41) Huang, M.; Luo, Z.; Zhu, T.; Chen, J.; Zhang, J. Z.; Xia, F. A. Theoretical Study of the Substituent Effect on Reactions of Amines, Carbon Dioxide and Ethylene Oxide Catalyzed by Binary Ionic Liquids. *RSC Adv.* **2017**, *7*, 51521–51527.

(42) Abbas, M. S.; Hussain, S.; Zhang, J.; Wang, B.; Yang, C.; Wang, Z.; Wei, Z.; Ahmad, R. Orientationally engineered 2D/3D perovskite for high efficiency solar cells. *Sustain. Energy Fuels* **2020**, *4*, 324−330.

(43) Dewick, P. M. *Essentials of Organic Chemistry: For Students of Pharmacy, Medicinal and Biological Chemistry*; Wiley: New York, 2006; p 146.